

Article

Confining He Atoms in Diverse Ice-Phases: Examining the Stability of He Hydrate Crystals through DFT Approaches

Raquel Yanes-Rodríguez [†]  and Rita Prosmi ^{*} 

Institute of Fundamental Physics (IFF-CSIC), CSIC, Serrano 123, 28006 Madrid, Spain; raquelyr@iff.csic.es

^{*} Correspondence: rita@iff.csic.es; Tel.: +34-91-5616800 (ext. 442292)[†] Doctoral Programme in Theoretical Chemistry and Computational Modelling, Doctoral School, Universidad Autónoma de Madrid, 28049 Madrid, Spain.

Abstract: In the realm of solid water hydrostructures, helium atoms have a tendency to occupy the interstitial spaces formed within the crystal lattice of ice structures. The primary objective of this study is to examine the stability of various ice crystals when influenced by the presence of He atoms. Presenting a first attempt at a detailed computational description of the whole energy components (guest–water, water–water, guest–guest) in the complete crystal unit cells contributes to enhancing the knowledge available about these relatively unexplored helium–water systems, which could potentially benefit future experiments. For this purpose, two different ice structures were considered: the previously established He@ice II system, and the predicted (but currently nonexistent) He@ice XVII system. One of the main features of these He-filled structures is the stability conferred by the weak van der Waals dispersion forces that occur between the host lattice and the guest atoms, in addition to the hydrogen bonds established among the water molecules. Hence, it is crucial to accurately describe these interactions. Therefore, the first part of this research is devoted examining the performance and accuracy of various semi-local and non-local DFT/DFT-D functionals, in comparison with previous experimental and/or high-level computational data. Once the best-performing DFT functional has been identified, the stability of these empty and He-filled structures, including different number of He atoms within the lattices, is analysed in terms of their structural (lattice deformation), mechanical (pressure compression effects) and energetic properties (binding and saturation energies). In this manner, the potential formation of these structures under zero temperature and pressure conditions can be evaluated, while their maximum storage capacity is also determined. The obtained results reveal that, despite the weak underlying interactions, the He encapsulation has a rather notable effect on both lattice parameters and energetics, and therefore, the guest–host interactions are far from being negligible. Besides, both ice crystals are predicted to remain stable when filled with He atoms, with ice XVII exhibiting a higher capacity for accommodating a larger number of guest atoms within its interstitial spaces.

Keywords: electronic structure calculations; DFT approaches; molecular interactions; gas hydrates; crystal He-filled ice phases



Citation: Yanes-Rodríguez, R.; Prosmi, R. Confining He Atoms in Diverse Ice-Phases: Examining the Stability of He Hydrate Crystals through DFT Approaches. *Molecules* **2023**, *28*, 7893. <https://doi.org/10.3390/molecules28237893>

Academic Editors: Donald G. Truhlar, Chiara Cappelli, Antonio Fernández-Ramos, M. Natália D.S. Cordeiro and Bryan M. Wong

Received: 3 November 2023

Revised: 24 November 2023

Accepted: 28 November 2023

Published: 1 December 2023



Copyright: © 2023 by the authors. Licensee MDPI, Basel, Switzerland. This article is an open access article distributed under the terms and conditions of the Creative Commons Attribution (CC BY) license (<https://creativecommons.org/licenses/by/4.0/>).

1. Introduction

Due to their small size and weak interaction with water molecules, helium atoms tend to occupy interstitial spaces within the crystal lattice of ice-like structures, such as hexagonal ice (I_h) or ice II, rather than forming stable clathrate-like structures [1–4]. Nonetheless, the information available about these He-filled structures is quite limited, with the helium–water system remaining relatively unexplored. Arnold et al. made a prediction in 1971 that helium could potentially enter the open channels of both ice I_h and ice II [5]. Prior to this, evidence for helium in ice I_h had already been discovered [6,7], and later solubility studies provided further confirmation [8–10]. It was not until 1988 that the first experimental evidence for the formation of helium inclusion compounds in ice II at pressures exceeding

0.28 GPa was presented by Londono et al. [1]. A few years later, a more detailed neutron diffraction experiment on this structure was conducted [2]. Lobban et al. expanded on the discussion of He-filled ice II by comparing it with refined neutron diffraction data for pure ice II [11]. In 2003, neutron-diffraction measurements on He-affected ice I_h samples were reported by Wang and Li [12]. New experimental data on He-filled ice I_h up to 120 bar were published in 2013 [13]. It was necessary to await until 2018 for the publication of novel data concerning the first experimental confirmation of helium inclusion in sII clathrate hydrate (ice XVI) and ice I_h. In the meantime, a few theoretical studies on pure He-filled ices [14–18], as well as computational and experimental findings in helium containing mixtures, have been published [19–22].

Despite the seemingly comprehensive research on He-filled ice crystals, there is actually a scarcity of valuable data on He@hydrate interactions. This deficiency motivates us to further expand the current knowledge available about such ice crystals in the presence of He atoms by investigating their stability through DFT computations. The selection of the He atom as a guest is driven not just by the limited research on helium hydrates, but also by its potential as a promising candidate for generating novel ice structures. The unique nature of He allows it to form interactions that can sufficiently stabilize certain inclusion compounds, and yet be weak enough to facilitate its removal from the host structure, thus enabling the stabilization/formation of new structures or the incorporation of alternative guest molecules [23]. This advantageous feature has already been harnessed in a Ne hydrate, where the Ne atoms initially stabilized the sII clathrate hydrate and were subsequently extracted, resulting in the formation of ice XVI [24].

Within this context, computational investigations emerge as advantageous tools that hold the potential to guide and accelerate the discovery of novel materials and reactions [25–29]. The availability of high-performance computing platforms and supercomputers empowers researchers to address computationally intensive tasks, such as molecular dynamics simulations, electronic structure calculations, and chemical reaction modeling [30–33]. Moreover, the development and implementation of diverse quantum chemistry methodologies, such as density functional theory (DFT), *ab initio* electronic structure methods, and machine learning approaches, have expanded the scope of chemical systems that can be studied with unprecedented precision and efficiency [34–37]. Thus, a wide range of properties can be explored, offering insights into the structure, energetics, spectroscopy or reactivity of molecules, materials and reactions.

Hence, building upon our previous endeavours in studying the stability of helium clathrate hydrates [38–40], our current research focuses on examining the impact of confining He atoms within the channels of ice crystals through DFT computations. To this end, two different types of ices were selected: ice II, which has already been experimentally observed in the presence of He atoms [2], and a recently discovered form of ice, known as ice XVII [41], which has been successfully filled with Ne atoms in the laboratory [42]. This novel structure has garnered the attention of numerous researchers [43–47], and since there is no absolute understanding of its stability in the presence of helium atoms, we have opted to include it in our study. As far as we are aware, this is the first time that theoretical data on its stability will be provided. Hence, this study is a first attempt to describe, through first-principles computations, the interactions (guest–guest, guest–host, host–host) that govern the stability of these ice crystals in the presence of He atoms in terms of structural, mechanical, and energetic properties. Furthermore, we will also delve into the effects of multiple occupancy, aiming to determine the maximum storage capacity of these systems.

2. Results and Discussion

This investigation is divided into two distinct parts. The first part involves a benchmark study on the crystal structures of ice II and ice XVII. The objective is to evaluate the performance of different DFT-D functionals that have been recognized as effective in describing ices and clathrate hydrates in the literature [38,45,48–54]. In addition, the benchmark study encompasses ice II and ice XVII structures containing one or multiple

He atoms, respectively, alongside their respective empty ice II/ice XVII lattices, in order to consider the impact of an increasing number of He atoms occupying the interstitial spaces within the ice lattices. Once the most suitable DFT-D functional for accurately describing the interactions in ices has been determined, the second part of the investigation focuses on analyzing the stability of ice II and ice XVII frameworks. To identify the most favorable configuration, several He-fillings are considered, each involving a different number of He atoms that occupy the voids.

2.1. Simulation Cells, Computational Details and Lattice Energies

In Figure 1 the *c*-axis view of the two structures under study is depicted. Ice II is a proton-ordered form of ice, composed of two different types of hexagonal water rings, one chair-form and one almost flat, which are alternatively stacked along the *c*-axis, forming columns with interstitial spaces between rings [55]. The hexagonal unit cell ($R\bar{3}$ space group), with lattice parameters $a = b \neq c$ and angles $\alpha = \beta = 90^\circ$ and $\gamma = 120^\circ$, is formed by 36 water molecules. The structure of ice XVII is characterized by hexagonal helices that spiral along the *c*-axis. These helices are constructed from sheets that consist of hydrogen-bonded pentagonal water rings. The hexagonal unit cell ($P6_122$ space group) is formed by a water pentamer hydrogen-bonded to a water molecule. Their structures were determined by neutron diffraction experiments and reported in refs. [2,43], respectively. Various configurations containing a varying number of He atoms were also considered. One, two and three He atoms are confined within the voids of ice II, identified as $\text{He}_{(1)}@$ ice II ($\text{H}_2\text{O}:\text{He}$ ratio, called hydration number, 36:6), $\text{He}_{(2)}@$ ice II ($\text{H}_2\text{O}:\text{He}$, 36:12) and $\text{He}_{(3)}@$ ice II ($\text{H}_2\text{O}:\text{He}$, 36:18), respectively. Since the ice XVII channels have a zig-zag form, we will distinguish between two types (right/left) of interstitial spaces. Thus, $\text{He}_{(1/1)}@$ ice XVII ($\text{H}_2\text{O}:\text{He}$, 6:2), $\text{He}_{(1/2)}@$ ice XVII ($\text{H}_2\text{O}:\text{He}$, 6:3), $\text{He}_{(2/2)}@$ ice XVII ($\text{H}_2\text{O}:\text{He}$, 6:4) and $\text{He}_{(3/3)}@$ ice XVII ($\text{H}_2\text{O}:\text{He}$, 6:6) are contemplated.

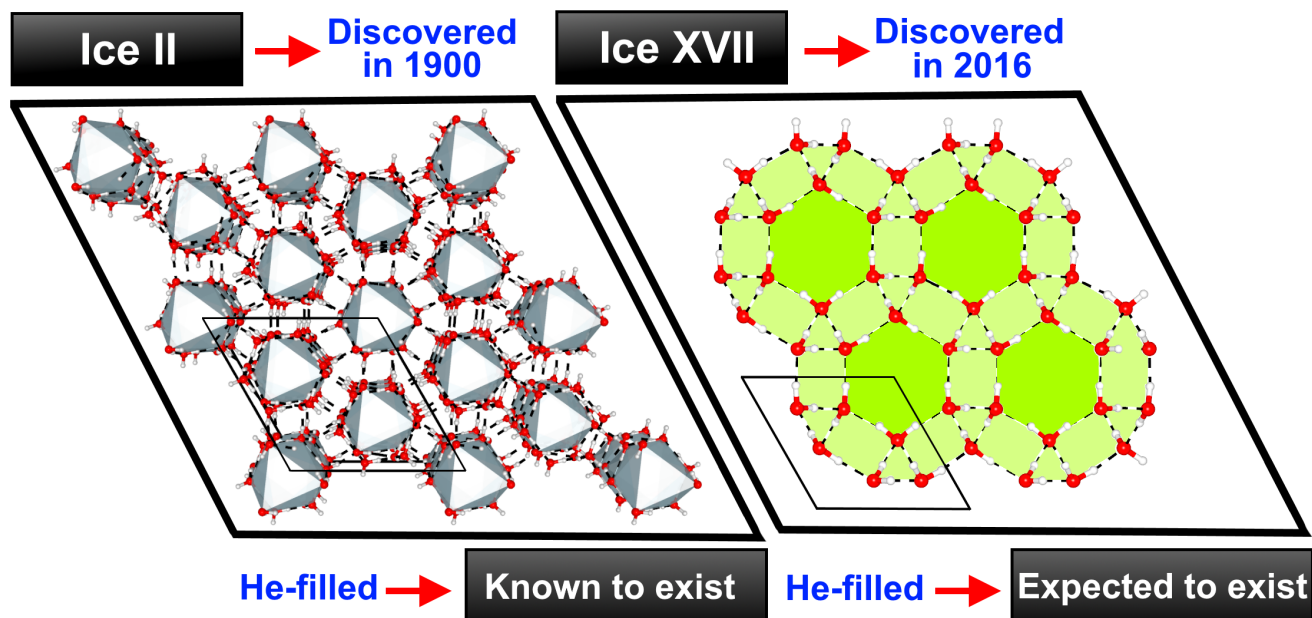


Figure 1. View along *c*-axis of ice II and ice XVII unit cells and corresponding extended crystal systems (plotted using VESTA [56]), with oxygen, hydrogen atoms in red and white color, respectively, while hydrogen bonds are shown as black lines.

Electronic structure DFT calculations were performed for both empty and He-filled ice II and ice XVII structures using the QE code [57–59]. A benchmark study is first carried out including the semi-local exchange–correlation PW86PBE [60,61] and revPBE [62] GGA (generalized gradient approximation) functionals, along with the XDM [63,64] and

D3(0) [65] dispersion schemes as implemented in QE, and the D4 correction as a post-processing tool through the DFT-D4 program [66–69], as well as the non-local van der Waals-inclusive optB88-vdW [70], vdW-DF [71] and vdW-DF2 [72] functionals, with the dispersion contribution as an integral part of the exchange-correlation interaction. In this way, we investigate few selected functionals with different exchange-correlation expressions, as well as dispersion-correction schemes. The plane-wave pseudopotential approach within the projector-augmented-waves (PAW) method [73] was employed using the standard PBE-based pseudopotentials supplied within QE. Moreover, several single-point runs were carried out to check the convergence of the energy cutoff for the plane-wave expansion of the wave functions, $E_{\text{cut_wfc}}$, and for the charge density, $E_{\text{cut_rho}}$, resulting in a selection of 360/440 Ry (4898/5986 eV) for $E_{\text{cut_wfc}}$ and 90/100 Ry (1224/1360 eV) for the $E_{\text{cut_rho}}$ for the empty and He-filled ice II/ice XVII structures, respectively. A Monkhorst-Pack $2 \times 2 \times 2/6 \times 6 \times 6$ k-point grid [74] in the reciprocal space was used per unit cell in the ice II/ice XVII systems, while calculations for the isolated He and H₂O molecules were performed at the Γ -point in a cubic simulation cell of volume $30 \times 30 \times 30 \text{ \AA}$, considering the Makov–Payne method [75] of electrostatic interaction correction for these aperiodic systems. As for the geometry optimizations, all atomic positions were relaxed using the the Broyden–Fletcher–Goldfarb–Shanno (BFGS) quasi-newton algorithm with convergence criterion for the components of energy and forces being smaller than 10^{-4} Ry (10^{-3} eV) and 10^{-3} Ry/bohr (10^{-2} eV/bohr), respectively.

The cohesive energies per water molecule for the He-filled ices were calculated as:

$$\Delta E_{\text{coh}}^{\text{He}_N@ice} = \frac{E_{\text{opt}}^{\text{He}_N@ice}(a; c) - M \cdot E^{\text{H}_2\text{O}} - N \cdot E^{\text{He}}}{M}, \quad (1)$$

where $E_{\text{opt}}^{\text{He}_N@ice}(a, c)$ is the total energy of the occupied He_N@ice unit cell obtained by structural relaxation at each lattice constants a and c , $E^{\text{H}_2\text{O}}$ and E^{He} are the total energies of the isolated ground-state H₂O molecules and He atoms, respectively, M is the total number of water molecules ($M = 36/6$ for ice II/ice XVII) and N corresponds to the total number of He atoms, which in this case corresponds to $N = 6/12/18$ for the He₍₁₎@ice II, He₍₂₎@ice II and He₍₃₎@ice II and $N = 2/3/4/6$ for the He_(1/1)@ice XVII, He_(1/2)@ice XVII, He_(2/2)@ice XVII and He_(3/3)@ice XVII configurations, respectively.

Regarding the empty ice crystals, the cohesive energy is equivalently computed as:

$$\Delta E_{\text{coh}}^{\text{ice}} = \frac{E_{\text{opt}}^{\text{ice}}(a', c') - M \cdot E^{\text{H}_2\text{O}}}{M}, \quad (2)$$

where $E_{\text{opt}}^{\text{ice}}(a', c')$ stands for the optimized total energy of the empty ice unit cells at the different values of lattice constants a' and c' . Another energetic term used to analyse the stability of these compounds is the binding energy resulting from the encapsulation of the He atoms in the empty ice systems, which is given by

$$\Delta E^{\text{He}_N@ice} = E_{\text{opt}}^{\text{He}_N@ice}(a_0, c_0) - E^{\text{ice}}(a_0, c_0) - N \cdot E^{\text{He}} \quad (3)$$

where $E_{\text{opt}}^{\text{He}_N@ice}(a_0, c_0)$ corresponds to the total energy of the occupied He_N@ice structures obtained via structural relaxation at the equilibrium lattice constants a_0 and c_0 , and $E^{\text{ice}}(a_0, c_0)$ is the total energy of the empty crystals at the equilibrium lattice constants a_0 and c_0 . This quantity is also given in a per He atom basis. Finally, the energy corresponding to the saturation of all the channels in the ices, at a_0 and c_0 , is calculated as:

$$\Delta E_{\text{sat}} = E_{\text{opt}}^{\text{He}_N@ice}(a_0, c_0) - E_{\text{opt}}^{\text{crystal}}(a_0, c_0) - E_{\text{opt}}^{\text{N}\cdot\text{He}}(a_0, c_0), \quad (4)$$

where $E_{\text{opt}}^{\text{N}\cdot\text{He}}(a_0, c_0)$ is the total energy of the entire number of He atoms obtained by structural relaxation at the equilibrium lattice constants, a_0 and c_0 .

2.2. Benchmarking DFT-D Calculations

The semi-local revPBE and PW86PBE functionals were examined, along with the optB88-vdW, vdW-DF and vdW-DF2 functionals in order to investigate the impact of non-local dispersion effects. Dispersion corrections, such as those obtained from the XDM, D3(0) and D4 schemes [63–65,67–69], were also considered. For this purpose, geometric optimizations of all atomic positions of both He-filled and empty crystal structures of ice II and ice XVII were computed. In the case of ice II, the structure is filled with only one 1 He per interstitial space He₍₁₎@ice II, while ice XVII contains 3 He atoms per void He_(3/3)@ice XVII. In this manner, we can assess the effectiveness of the DFT functionals under three distinct conditions: empty structures (host–host interactions), structures filled with a single He atom per interstice (guest–host interactions), and structures filled with multiple He atoms (guest–guest interactions).

Full geometry optimizations were performed through DFT/DFT-D computations on the empty and He-filled ice structures at various lattice parameters, *a*, while keeping the crystal atomic radius between the *c* and *a* lattice parameters ($r = c/a$) constant. Before carrying out the whole benchmark study, total energies at a wide range of *r* and *a* values were calculated employing only the PW86PBE/-XDM/-D4 functional (given its lower computational cost), so as to identify the most energetically favourable *r* curve for both the empty and He-filled ice II and ice XVII systems. Specifically, the values of *r* and *a* for ice II/He₍₁₎@ice II and ice XVII/He_(3/3)@ice XVII were chosen to be within the ranges of 0.46–0.50 and 12.0–14.6 Å, and 0.94–0.98 and 5.8–7.4 Å, respectively. Figure S1 in the Supplementary Material shows the cohesive energies per water molecule plotted against *a* for different *r* values, with $r = 0.48$ and $r = 0.96$ yielding the lower energy curves for the empty/He-filled ice II and ice XVII structures, respectively, despite the difference between the curves at various *r* values being insignificant.

Therefore, hereafter, we focus the benchmark analysis on $r = 0.4816/0.4838$ (readjusted on the basis of experimental values [2,43]) for ice II/He₍₁₎@ice II, and $r = 0.96$ for both ice XVII and He_(3/3)@ice XVII. Figure 2 displays the cohesive energies per water molecule computed with the whole set of semi-local and non-local DFT functionals for both He-filled and empty ice structures. The DMC and/or experimental values available in the literature [2,43,76] are used as a guideline for elucidating the best-performed functional. Two characteristics are noteworthy from the analysis of these plots. On the one hand, it is observed that the vdW-DF and vdW-DF2 functionals cause the curves to shift towards larger *a* values, as expected due to their ability to account for long-range van der Waals interactions, which results in an increase in the equilibrium distance between particles. This effect is pronounced in He-filled and empty ice II, as well as in He_(3/3)@ice XVII. On the other hand, although the inclusion of He atoms barely has any effect on the lattice of ice II, their presence in ice XVII has a significant impact. Thus, a displacement of the curve to larger *a* values is observed, indicating lattice expansion. This expansion suggests that the six He atoms within the interstitial spaces in the channel exert a repulsive effect.

In turn, with the aim of obtaining the equilibrium lattice constants, *a*₀, *c*₀ (or *a*'₀, *c*'₀), and the corresponding equilibrium cohesive energies, the calculated total energies for the He-filled and empty ices as a function of the lattice constant *a* and crystal atomic radius *r* are fitted to the Murnaghan's equation of state (MEOS) [77] (see solid lines in Figure 2), which represents a relation between the volume and the energy, $E(V) = E_0 + B_0 V_0 \left[\frac{1}{B_0(B_0 - 1)} \left(\frac{V}{V_0} \right)^{1 - B_0'} + \frac{1}{B_0'} \frac{V}{V_0} - \frac{1}{B_0' - 1} \right]$, where *B*₀ and *B*'₀ are the modulus of incompressibility and its first derivative with respect to the pressure, respectively.

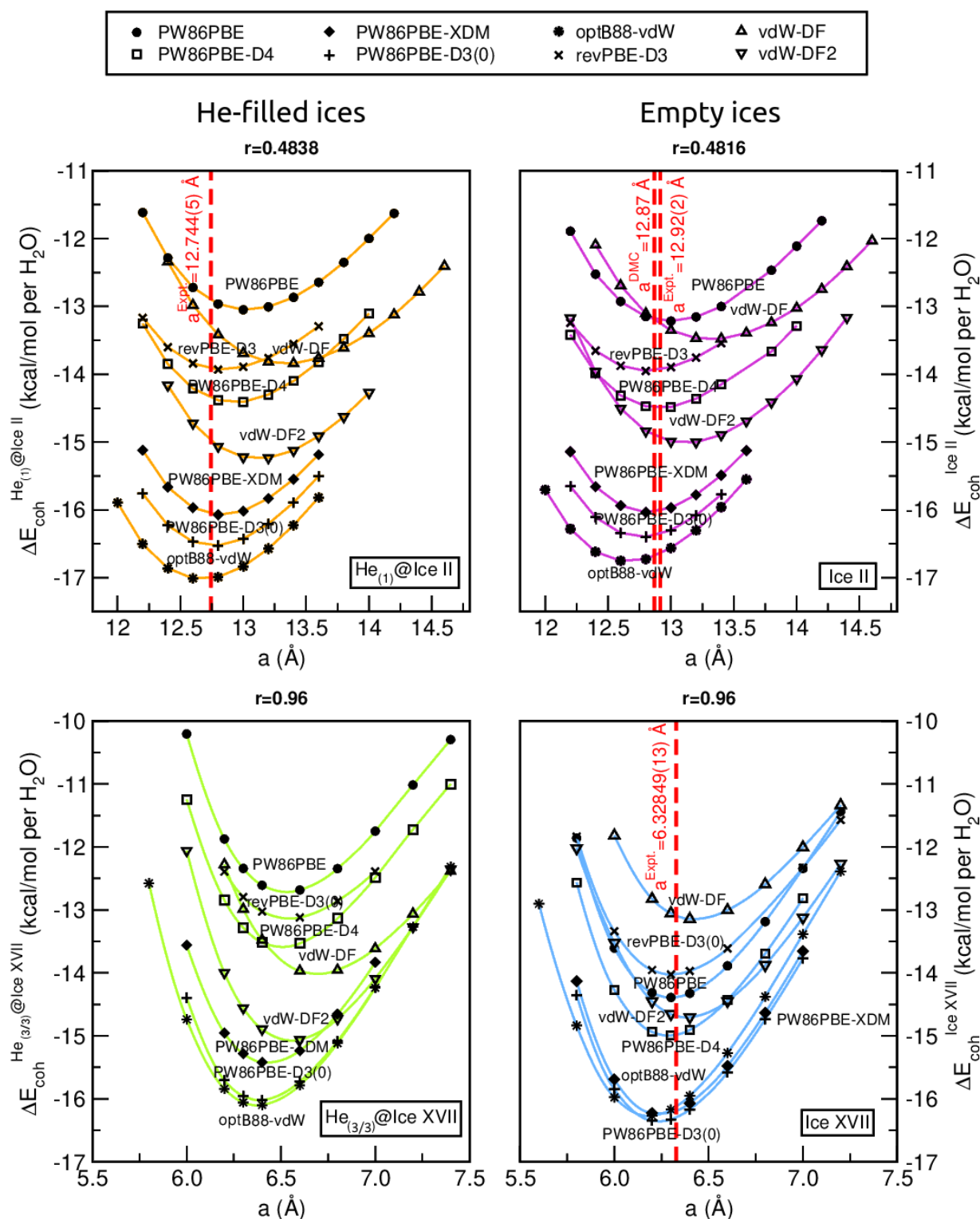


Figure 2. Cohesive energies, in kcal/mol per water molecule, of the $\text{He}_{(1)}@ \text{ice II}$ (upper panels) and $\text{He}_{(3/3)}@ \text{ice XVII}$ (lower panels) crystalline structures, together with their empty analogs, as a function of the lattice constant a and crystal atomic radius r values. Solid lines corresponds to the MEOS fits, while the values of experimental/theoretical equilibrium lattice constants are drawn with vertical red dashed lines. See Refs. [2,76] for experimental values extrapolating at zero T-P conditions for the $\text{He}@ \text{ice II}$ and ice II, respectively, and Ref. [76] for the DMC value of ice II. The experimental value for ice XVII at $T = 25$ K is taken from Ref. [43].

The resulting equilibrium lattice parameters, as well as equilibrium energies and bulk moduli (B_0 and B'_0 at zero pressure) are listed in Table S1 in the Supplementary Material. As discussed above, the vdW-DF and vdW-DF2 overestimate the a_0 constants, yielding values ~ 0.5 and 0.3 Å larger than the $\text{He}_{(1)}@$ ice II/ice II experimental ones (12.74/12.92 Å) [2,76], respectively, and ~ 0.1 Å larger than the ice XVII experimental one (6.33 Å) [43]. In fact, among the methods evaluated, vdW-DF followed by vdW-DF2 and optB88-vdW show the highest % error. In contrast, revPBE-D3(0) exhibits the smallest average % error (0.6%), deviating from the experimental values by only 0.1 Å for $\text{He}_{(1)}@$ ice II/ice II and 0.03 Å for ice XVII. The PW86PBE, PW86PBE-D4 and PW86PBE-D3(0) functionals proportionate to the closest values for ice XVII, ice II and $\text{He}_{(1)}@$ ice II, respectively.

Moving forward with the assessment, Figure 3 illustrates the percentage error concerning, as a reference, the $-12.916/-13.781$ kcal/mol DMC $\Delta E_{coh}(a'_0, c'_0)$ energies for ice II/ice XVII [53]. Curiously, despite the fact that non-local functionals overestimate the lattice constant, they provide fairly accurate equilibrium energies. The functionals PW86PBE-XDM, PW86PBE-D3(0), and optB88-vdW exhibit the most significant energy underestimation, predicting values that are 2.3–2.6 kcal/mol lower than the DMC calculations. In this case, it is clearly evident that the functional which predicts the most precise energies is once again the revPBE-D3(0), being the deviation from the reference value of a mere 0.2 kcal/mol (1.4% average error).

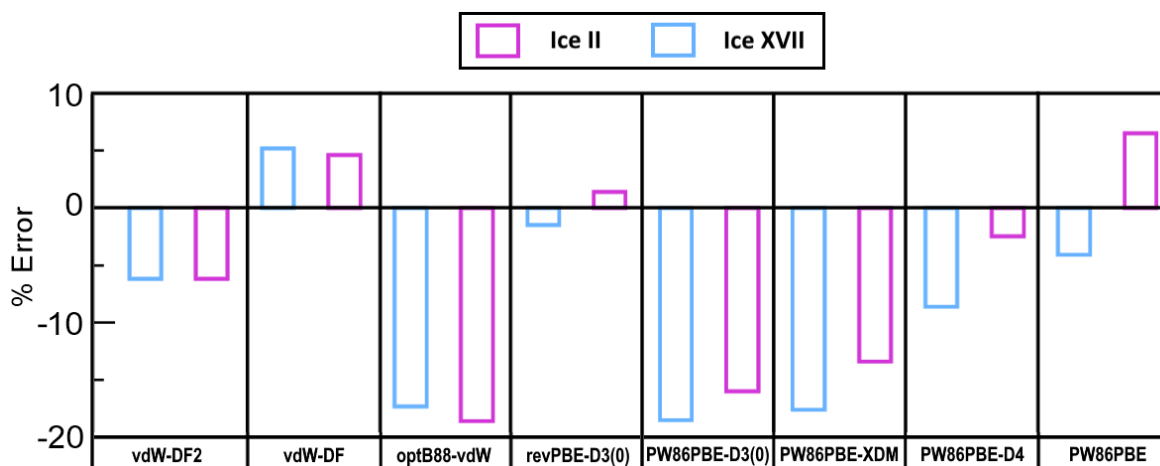


Figure 3. Error (in %) with respect to the computationally reported $\Delta E_{coh}(a'_0, c'_0)$ values of $-12.916/-13.7814$ kcal/mol from DMC calculations for ice II/ice XVII [53].

To complete this analysis, we also discuss the B_0 and B'_0 parameters, which characterize the response of a material to uniform compression, as shown in Table S1 in the Supplementary Material. They are estimated from the corresponding MEOS fits, assuming linear dependence of the bulk modulus with pressure, $B = B_0 + B'_0 \times P$, with B_0 being constant and valid for the range $B'_0/2 > P > 0$. Thus, we observe that, with the exception of PW86PBE and PW86PBE-D4, all the functionals predict that B_0 is greater for the He-filled structure compared to the empty one, indicating that $\text{He}_{(1)}@$ ice II is more rigid and resistant to compression than ice II, although the difference between both B_0 values is rather small.

In turn, Lobban et al. [11] reported an isothermal bulk modulus of 14.8 GPa and 20.6 GPa for the empty and He-affected ice II structures at 200 K and 196 K, respectively. Therefore, an increase in B_0 is expected when the ice is filled with He atoms. This can be attributed to the resistance offered by the helium atoms located within the c -axis channels against any external compression. As for the numerical values, we found that our B_0 and B'_0 results are in line with previously reported zero-temperature and zero-pressure *ab initio* PW91 calculations [78], where $B_0 = 16.18 \pm 0.12$ GPa, with the first pressure derivative of the bulk modulus, B'_0 , fixed equal to 6.0. Previous experimental values yielded $B_0 = 14.39$ GPa for H_2O ice II at 0.283 GPa and 237.65 K [79], $B_0 = 14.8$ GPa for D_2O ice II at 0.35 GPa and

200 K [11], and $B_0 = 14.23$ GPa for D_2O ice II at 0.35 GPa and 225 K [80]. Accordingly, the revPBE-D3(0) provides the most accurate results. On the contrary, with regards to ice XVII, there are more discrepancies. While PW86PBE, along with any dispersion scheme, and optB88-vdW DFT functionals estimate that the He-filled ice XVII is more compressible and less stiff than the empty ice XVII, the revPBE, vdW-DF and vdW-DF2 functionals suggest that B_0 is smaller for the ice XVII, and therefore, it is less resistant to compression. Unfortunately, there is no available information in the literature regarding the response of this structure to compression. Hence, we cannot determine which of the observed trends is the expected one.

In conclusion, based on all the aforementioned information, we consider that the exchange-correlation revPBE-D3(0), which is constrained by exact functional conditions with a posteriori incorporation of the D3 dispersion corrections, is the functional that provides a better description of the interactions in both empty and singly/multiply-filled ice structures, in line with previous high-level theoretical and experimental reports on ice polymorphs [53] and interfacial water [81].

2.3. Influence of Increasing Number of He Atoms on Ice Crystal Properties

2.3.1. Structural and Mechanical Analysis

To investigate the capacity of ice II and ice XVII structures and understand how the lattice deforms as the number of He atoms increases, different ice crystals with varying He-fillings are studied by carrying out revPBE-D3(0) calculations. In particular, in addition to the already discussed $He_{(1)}@ice$ II (1 He atom/interstice) and $He_{(3/3)}@ice$ XVII (3 He atoms/interstice) systems, the $He_{(2)}@ice$ II (2 He atoms/interstice), $He_{(3)}@ice$ II (3 He atoms/interstice), $He_{(1/1)}@ice$ XVII (1 He atoms/interstice), $He_{(1/2)}@ice$ XVII (1–2 He atoms/interstice) and $He_{(2/2)}@ice$ XVII (2 He atoms/interstice) were also examined.

Following a similar procedure to that explored in the above-mentioned benchmark study, full geometry optimisation calculations were first carried out at revPBE-D3(0) level of theory for fixed values of r ($r = 0.4838/0.96$ for He-filled ice II/ice XVII, respectively), within the same range of values. Subsequently, the computed optimized total energies were fitted to the MEOS, and a_0 , c_0 , $\Delta E_{coh}(a_0; c_0)$ and B_0/B'_0 were obtained. The corresponding results are graphed in Figures 4 and 5, along with the findings obtained for the empty crystal in the preceding section. Numerous observations merit further discussion. When considering the ice II structure (see upper panels of Figure 4 and left-side panels of Figure 5), it is notable that the introduction of a single He atom per interstitial space barely affects the lattice; however, the addition of multiple He atoms results in significant changes to the crystal, which tends to expand in order to mitigate the repulsion generated by the He atoms in the confined space. The numerical analysis reveals that the equilibrium lattice constant for the empty ice II crystal differs from that of the He-filled $He_{(1)}@ice$ II, $He_{(2)}@ice$ II, and $He_{(3)}@ice$ II structures by 0.03, 0.35 and 0.63 Å, respectively.

The calculated lattice parameter $a_0 = 12.84$ Å for $He_{(1)}@ice$ II is the most proximal to the experimentally expected value of $a_0 = 12.744(5)$ Å for the He-filled ice II under zero T-P conditions [2]. This value comes from the proposed expression by Londono et al. [2] to establish a relationship between lattice constant, temperature and pressure: $a_0 = 12.744(5) - 0.036(5)P + 0.0009(1)T$. Nonetheless, since the comparison between the expected a_0 and a'_0 parameters at zero temperature and pressure is rather confusing ($a'_0 = 12.92(2)$ Å according to the extrapolation made by Santra et al. [76]), it seems more reasonable to discuss about the trends observed under comparable T-P regimes [11]. Thus, alterations of 0.01, 0.02 and 0.04 Å have been reported [11] at 2.8 kbar/200 K, 4.2 kbar/250 K and 4.8 kbar/200 K between the empty and He-filled ice II crystals, respectively, leading to the expansion of the ice structure upon the incorporation of He atoms. Our results are in line with these experimental observations.

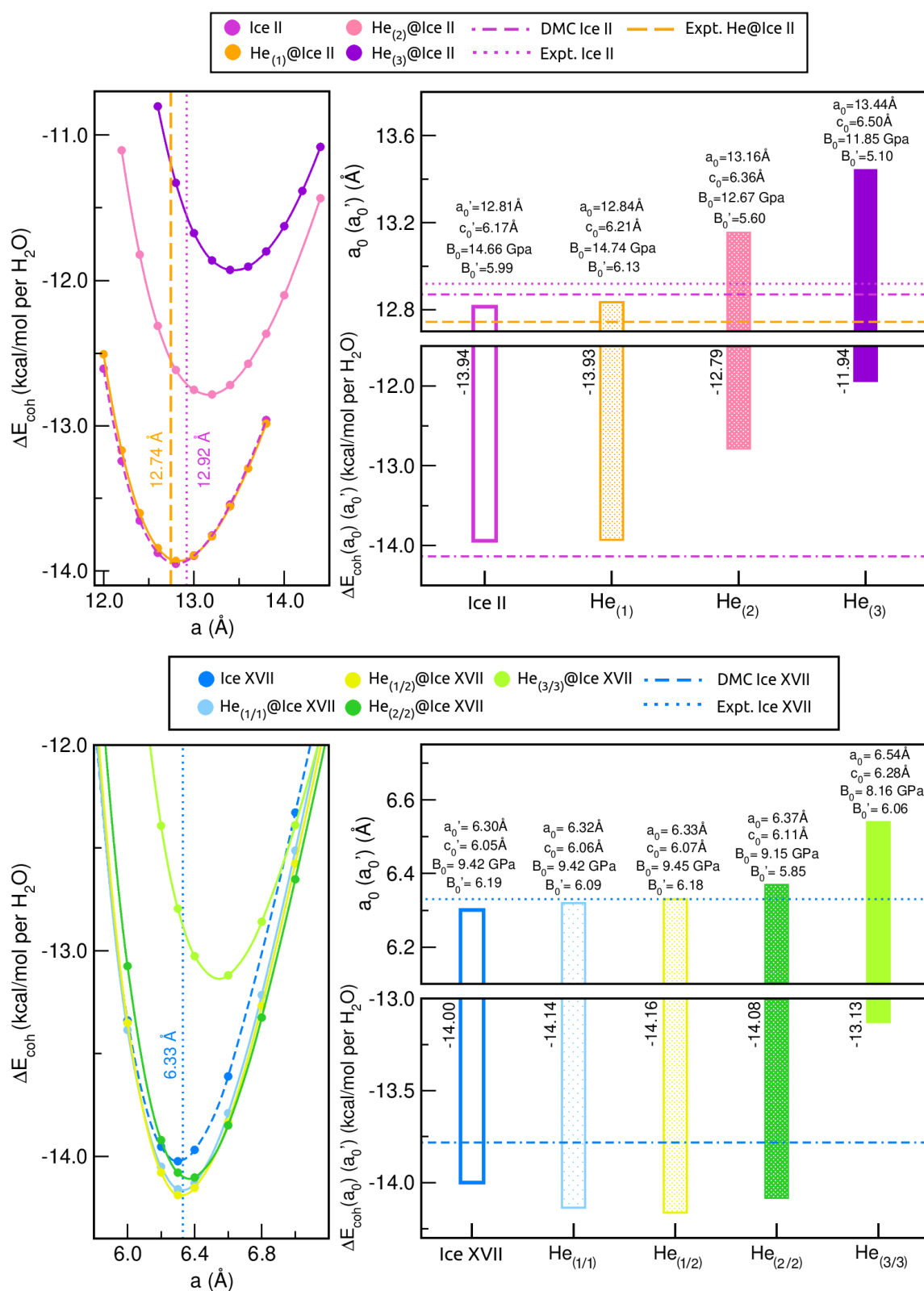


Figure 4. Cohesive energies (per water molecule) in kcal/mol at various values of a lattice constants for fixed values of r ($r = 0.4816/0.4838$ for empty/He-filled ice II and $r = 0.96$ for both empty/He-filled ice XVII) from revPBE-D3(0) calculations, and comparison of the resulting equilibrium a'_0 or a_0 and $\Delta E_{coh}(a'_0; c'_0)/(a_0; c_0)$ parameters with the available theoretical/experimental data [2,43,53,76] for the empty and He-filled ice II (upper panels) and ice XVII (lower panels). The bulk moduli is also indicated.

Further analysis of our equilibrium cohesive energies (per water molecule) also reveals the same conclusions. While the inclusion of one He between two hexagons along the *c*-axis has a negligible effect on the crystal, the incorporation of additional He atoms seems to be less favourable, with a difference of ~ 1 and 2 kcal/mol for He₍₂₎@ice II and He₍₃₎@ice II, respectively, compared to the empty system. As for the bulk modulus, B_0 , filling ice II with He atoms is expected to be accompanied by an elevation in B_0 due to the resistance exerted by the noble gas atoms under the application of external pressure [11]. This phenomenon is fulfilled when comparing the results from ice II and He₍₁₎@ice II crystals; however, as additional He guests are included, a gradual decrease in B_0 is identified, resulting in structures that are more easily deformable.

In contrast to ice II, we distinguish a less notorious He-filling effect in ice XVII, with the He_(1/1)@ice XVII and He_(1/2)@ice XVII lattices being only 0.02 and 0.03 Å larger than the empty one, respectively (see lower panels of Figure 4 and right-side panels of Figure 5). Incorporating 2 He atoms per interstitial space (He_(2/2)@ice XVII) becomes more noticeable, with a size increase of 0.07 Å, whereas the introduction of three He atoms per void (He_(3/3)@ice XVII) significantly affects the lattice by expanding it by 0.24 Å. Nonetheless, the effect is still comparatively lower than in ice II, possibly because of the wider diameter of the channels present in ice XVII, which facilitates a higher He occupancy. In the absence of any additional experimental or theoretical data for He-filled ice XVII, we can draw comparisons between our findings and those reported for Ne@ice XVII [42]. Catti et al. [42] have compared the structures of the D₂O framework in empty and Ne-filled ice XVII, and they have reported that Ne absorption at 50 K resulted in a significant expansion of 0.05 Å of *c* and a small contraction in the *a* lattice constant of approximately 0.01 Å; these changes are likely due to the Ne-D repulsion effects and the attractive van der Waals interactions between Ne and O, respectively. Here, in all the examined He@ice XVII structures, the incorporation of He atoms into the ice XVII channels results in lattice expansion, which can be attributed to the comparatively higher polarisability of Ne atoms compared to He. Such lattice expansion ensues an overall volume increase of 1.4 Å³ in the He_(1/1)@ice XVII, which is in accord with that of $+1.1$ Å³ reported in partially Ne-filled deuterated ice XVII [42].

Regarding comparisons of the equilibrium cohesive energies (per water molecule) of He_(1/1)@ice XVII, He_(1/2)@ice XVII, and He_(2/2)@ice XVII to the empty crystal, we found that they are more favourable by 0.14 , 0.16 , and 0.08 kcal/mol, respectively, while the energy difference relative to He_(3/3)@ice XVII is 0.87 kcal/mol less energetically favoured. Therefore, while in ice II, the energies were almost identical (with only a 0.01 kcal/mol difference), the inclusion of up to 2 He atoms per interstice in ice XVII results in a more significant stabilization of the complex. Finally, we found that the bulk modulus of ice XVII and He_(1/1)@ice XVII is equivalent, whereas for He_(1/2)@ice XVII, it slightly increases, indicating a more rigid structure. Incorporating additional He atoms leads to more flexible systems (lower B_0 values), which is particularly noticeable in He_(3/3)@ice XVII. Overall, based on this analysis, it seems that He_(3/3)@ice XVII is the least favoured structure, and has a considerable impact on the lattice in terms of its structural, energetic, and mechanical properties.

In Figures S2 and S3 of the supplementary material, the average H₂O-H₂O and He-He bond lengths for all the empty and He-filled ice II and ice XVII crystals are displayed, respectively. The ice II structure is formed of two different types of water hexagons, one with a larger average distance between opposite water molecules (flat ring), but a smaller distance between adjacent water molecules, while the other exhibits the opposite behaviour (puckered ring). Consistent with our previous analysis, we have found that there are negligible differences between the empty ice II structure and the He-filled He₍₁₎@ice II system (see Figure S2). This suggests that the introduction of a single He atom per interstitial space has almost no impact on the lattice. Londono [2] and Lobban [11] have reported values for the diameter of the hexagonal rings at similar T-P conditions, finding that the He-affected flat rings were 0.04 – 0.05 Å larger than the unaffected ones, whereas the puckered

rings remained almost unaltered. Similar observations were encountered for Ne-filled ice II lattices, where the insertion of Ne atoms resulted in an enlargement of the O-O distances and the channels diameter [82]. Our findings align with these observations, as we also predict a broadening of 0.02 Å in both rings when transitioning from the empty crystal to the He₍₁₎@ice II structure. The confinement of extra He atoms significantly affects these average distances, even leading to unit cell deformation in the case of He₍₃₎@ice II. Finally, an additional noteworthy feature is the positioning of the He atoms, which are situated approximately midway between the two distinct water hexagons, but with a slight displacement towards the flat ring. This aspect leads to the presence of one shorter and one longer He-He distance, in line with previous experimental findings [2].

The ice XVII structure presents wider channels, whatever the empty or He-filled system considered (see Figure S3). The average O-O bond length within water pentamers increases relative to the empty structure. Curiously, it is 0.11/0.13 Å larger for the He_(1/1)@ice XVII /He_(2/2)@ice XVII crystals, while only 0.01 Å in the case of He_(1/2)@ice XVII. The He_(3/3)@ice XVII system is much affected, with a distance increase of 0.55 Å. Equivalent to He₍₃₎@ice II, it seems that the accumulation of a great number of He atoms within the small confined space of He_(3/3)@ice XVII results in considerable repulsion and lattice distortion. The He atoms follow a spiral arrangement that conforms to the zig-zag shape of the channel. Overall, the interatomic distances found for He_(1/2)@ice XVII are comparable to, but smaller than, those reported for Ne@ice XVII (at 50 K) [42].

In turn, by using the calculated volume and bulk moduli, the pressure exerted on the ice lattices can be calculated according to the MEOS expression in terms of pressure as a function of the volume, such that $P(V) = \frac{B_0}{B'_0} \left[\left(\frac{V}{V_0} \right)^{-B'_0} - 1 \right]$. Figure 6 shows the volume as a function of the pressure for all the empty and He-filled ice crystals. It is well known that when a material is subjected to pressure, its volume decreases. Nevertheless, the degree of compression induced by pressure relies on the material's properties, such as its bulk modulus. As previously mentioned, the B_0 values encountered for ice XVII are lower than those of ice II. Consequently, it is expected that all the ice XVII structures will undergo a more significant change in volume under pressure, since they are less rigid, as confirmed in Figure 6. Besides, an increase in the number of confined He atoms results in structures that are more susceptible to compression, likely due to their reduced stability.

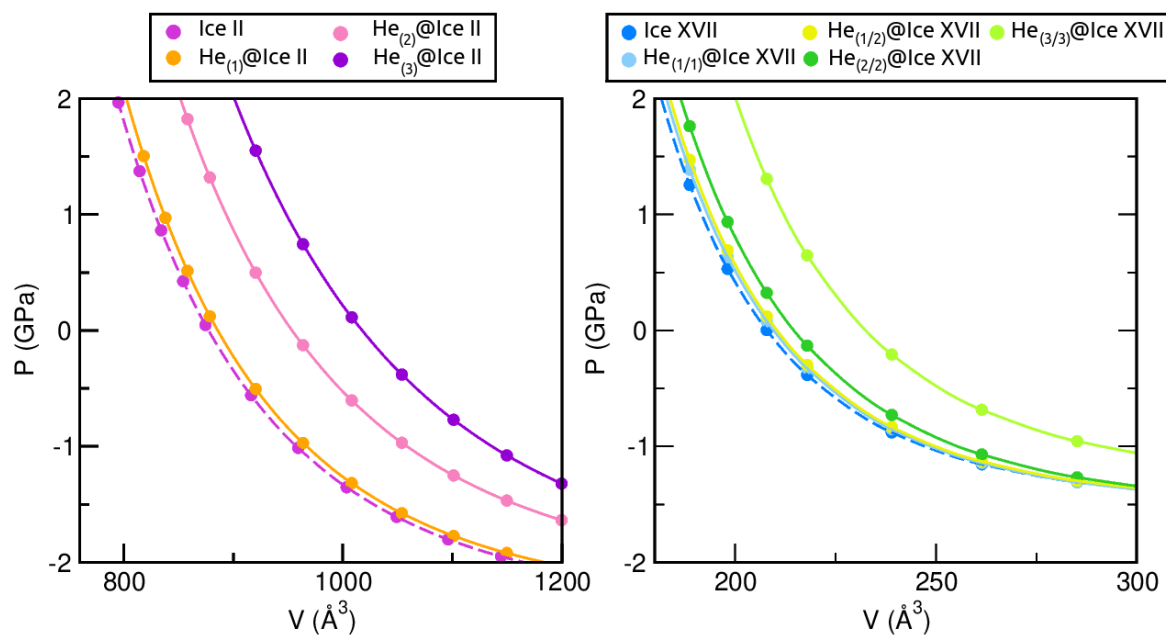


Figure 6. Pressure effects on the volume of the He-filled and empty ice II and ice XVII systems as determined from MEOS fits.

2.3.2. Energetic Analysis

The stability of these systems can be evaluated in terms of energy. To this end, the total binding energies of all the He-filled ices with respect to the guest-free systems are calculated, at the respective equilibrium lattice constants, a_0 and c_0 , using the revPBE-D3(0) approach. The corresponding energies are shown in Figure 7. Firstly, we observe that for ice II, the only favourable He-filled structure is that containing one He atom per interstitial void, while those entrapping 2 and 3 He atoms are predicted to be energetically unstable. This observation is not surprising, since it aligns with the outcomes that have been previously discussed. On the contrary, the whole set of He-filled ice XVII configurations is energetically favoured. In particular, little difference is observed between $\text{He}_{(1/2)}@ice XVII$, $\text{He}_{(2/2)}@ice XVII$ and $\text{He}_{(3/3)}@ice XVII$, with $\text{He}_{(1/2)}@ice XVII$ being the optimal structure, while $\text{He}_{(1/1)}@ice XVII$ is the less favourable one. The binding energy per He atom (see numerical results in Figure 7) decreases as the number of He atoms increases; this effect is more noticeable in both $\text{He}_{(2/2)}@ice XVII$ and $\text{He}_{(3/3)}@ice XVII$ structures.

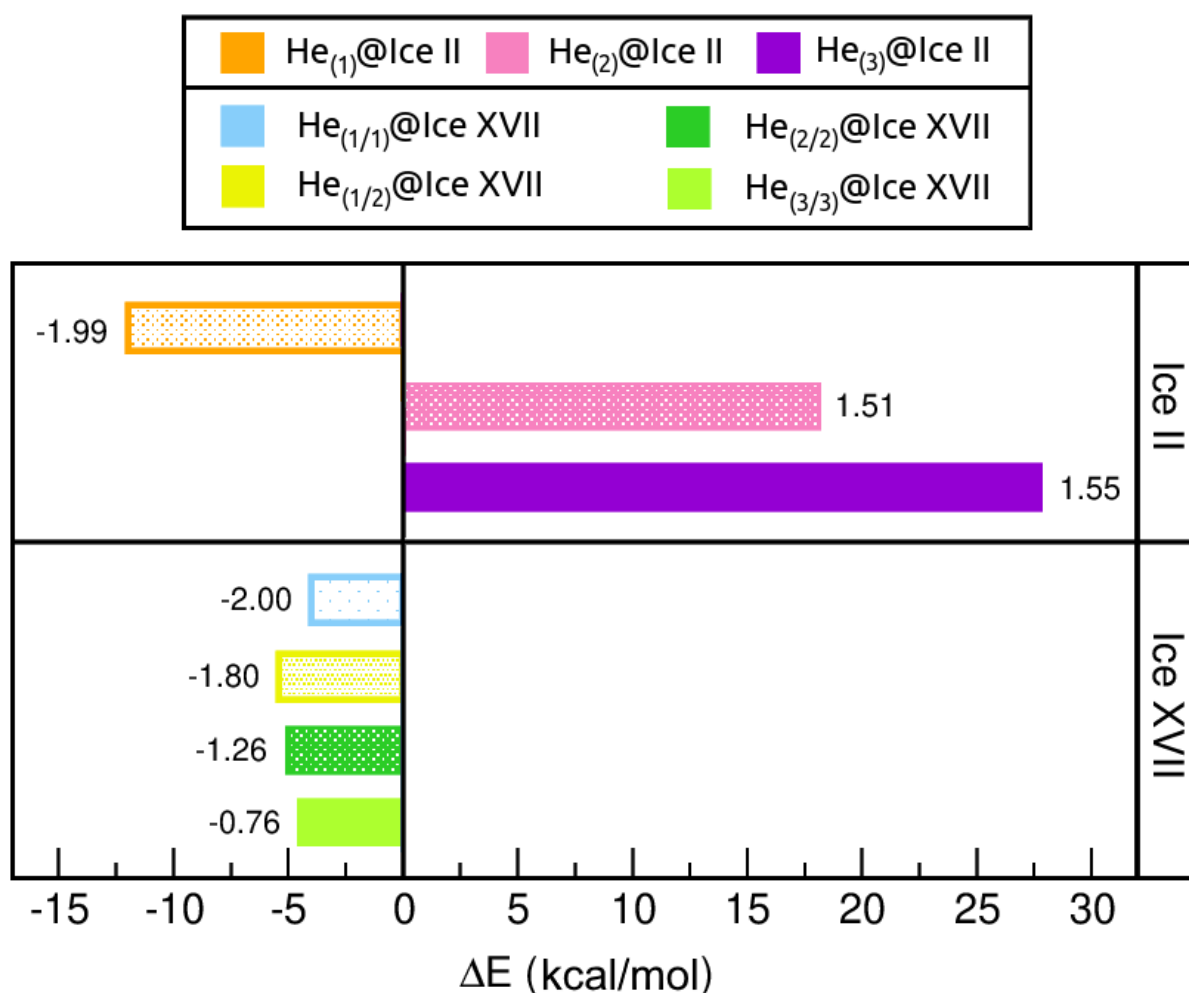


Figure 7. Binding energies, ΔE , in kcal/mol, for $\text{He}_N@ice II$ with $N = 1, 2, 3$ and $\text{He}_N@ice XVII$ with $N = (1/1), (1/2), (2/2), (3/3)$. ΔE per He atom values are indicated inside the plot with numbers. All calculations were performed using the revPBE-D3(0) DFT functional.

Further analysis of the stability entails the computation of the saturation energies for all He-filled structures, as illustrated in Figure 8. Such values provide an indication of the overall energy gain upon saturation of all channels, rather than just with respect to the addition of individual He atoms. In contrast to the binding energies, unfavourable ΔE_{sat} is predicted for all $\text{He}_N@ice II$ systems. However, its value is in close proximity

to zero for the $\text{He}_{(1)}@ice\ II$, while it experiences a sharp increase for $\text{He}_{(2)}@ice\ II$ and $\text{He}_{(3)}@ice\ II$, reaching values that indicate extreme instability. The $\text{He}_N@ice\ XVII$ ensembles remain stable for $N = (1/1)$, $(1/2)$ and $(2/2)$, presenting energies of similar magnitudes. Among them, $\text{He}_{(2/2)}@ice\ XVII$ exhibits the most favourable configuration. Conversely, the $\text{He}_{(3/3)}@ice\ XVII$ structure is estimated to be unstable, with a ΔE_{sat} value of 2.22 kcal/mol.

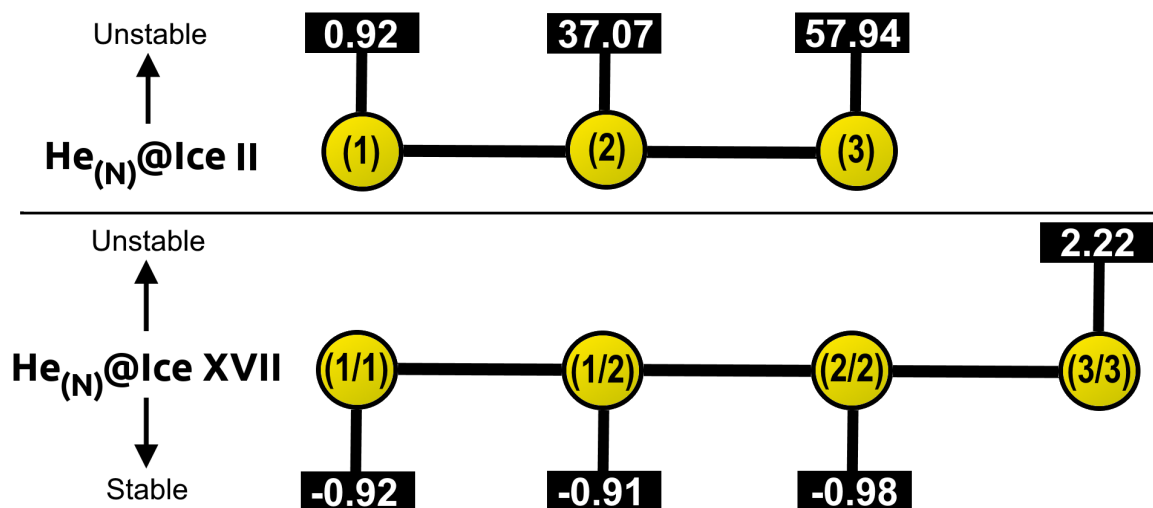


Figure 8. Saturation energies, ΔE_{sat} , in kcal/mol, for $\text{He}_N@ice\ II$ with $N = 1, 2, 3$ and $\text{He}_N@ice\ XVII$ with $N = (1/1), (1/2), (2/2), (3/3)$, as computed from the present revPBE-D3(0) calculations.

In general, considering the energetic and structural evaluation of both empty and He-filled ice II and ice XVII crystals, it seems that the ice II only may allow the inclusion of one He atom per interstitial space, while the ice XVII could accommodate up to two He atoms per void. It is important to consider that the present findings are applicable only under zero temperature and pressure conditions. According to the phase diagram of water, the ice XVII structure is situated in close proximity to these conditions. Hence, it is understandable that our calculations predict that the formation of He-filled ice II, which occurs under extremely high-pressure conditions, is less favourable.

3. Summary and Conclusions

This research focused on examining the behavior of crystalline ice structures confining an increasing number of He atoms. We have obtained valuable first-principles insights into the stability of two specific systems: the previously synthesized He@ice II, and a recent hypothetical He@ice XVII structure. First of all, we have conducted a benchmark study, including various semi-local dispersion-corrected GGA and non-local van der Waals-inclusive DFT-D functional approaches, in order to identify the most appropriate one that adequately describes the hydrogen bonds and van der Waals interactions inherent in these systems. Our findings indicate that the revPBE-D3(0) approach yields remarkably accurate results in comparison with available theoretical and/or experimental data. Benchmark studies on the performance of different DFT approaches can assist in resolving controversial issues and/or guide the development of novel/improved functionals.

In turn, the stability of different configurations of ice II and ice XVII structures with varying numbers of trapped He atoms within their channels was evaluated. The analysis primarily focused on examining structural, mechanical, and energetic properties, such as equilibrium lattice constants, resistance to compression, and binding/saturation energies. The presence of He atoms within the interstitial spaces of these systems has been observed to have a noteworthy impact. On the one hand, the ice II structure only accepts the inclusion of only one He atom per void, leading to minimal stabilization of the structure. The introduction of additional He atoms results in highly unstable configurations, causing even deformation of the lattice structure. On the other hand, the larger diameter of ice XVII

allows for inclusion of up to two He atoms per interstitial space. However, the confinement of extra guest atoms produces a destabilizing effect. Moreover, in contrast to ice II, the addition of just one He atom exerts a significant stabilizing effect on the lattice.

Overall, while both ice II and ice XVII structures are predicted to exhibit stability in the presence of He atoms, ice XVII demonstrates more stable configurations under zero temperature and pressure conditions. This observation aligns with the expected behavior in the phase diagram of solid water.

To further advance this line of investigation, additional studies can focus on several aspects. Vibrational properties can be explored by conducting phonon calculations to analyze the behavior of lattice vibrations within the He-confined ice structures. Furthermore, examining the response of these systems to variations in temperature and pressure would provide valuable insights into their thermodynamic stability and phase transitions. Molecular dynamics simulations can be employed to investigate the diffusion behavior of helium atoms within the channels, shedding light on their mobility and migration pathways. Understanding the stabilising role of He atoms in these solid hydrostructures holds great potential for the discovery of new low-density ices and materials.

Supplementary Materials: The following supporting information can be downloaded at: <https://www.mdpi.com/article/10.3390/molecules28237893/s1>. Figure S1: Cohesive energies of the He-filled (left panels) and empty (right panels) ice II and ice XVII as a function of the lattice constant a and ratio r . Symbols indicate the computed values from the PW86PBE/-D4/-XDM calculations, Figure S2: Average bond length and distances in Å for the empty and He-filled ice II structures considered in this study, Figure S3: Average bond length and distances in Å for the empty and He-filled ice XVII structures considered in this study, Table S1: MEOS fitting results obtained from semi-local and non-local DFT functionals for both He-filled and empty ice II and ice XVII.

Author Contributions: Conceptualization, R.P.; computations and software, R.Y.-R.; formal analysis and validation, R.Y.-R. and R.P.; writing—original draft preparation, R.Y.-R. and R.P.; writing—review and editing, R.Y.-R. and R.P.; visualization, R.Y.-R. and R.P.; supervision, R.P.; funding acquisition, R.P. All authors have read and agreed to the published version of the manuscript.

Funding: This research was funded by MCIN grant No. PID2020-114654GB-I00, Comunidad de Madrid grant No. IND2018/TIC-9467, and COST Actions CA18212(MD-GAS) and CA21101(COSY).

Institutional Review Board Statement: Not applicable.

Informed Consent Statement: Not applicable.

Data Availability Statement: The data supporting reported results are available from the corresponding author upon request. Cohesive energies and parameters obtained from the MEOS fitting to semi-local and non-local DFT functionals for both both He-filled and empty ice II and ice XVII are available online at <https://www.mdpi.com/article/10.3390/molecules28237893/s1>.

Acknowledgments: The authors thank M. Chaplin for providing the coordinates of ice XVII. The authors acknowledge the Centro de Cálculo del IFF, SGAI (CSIC) and CESGA for allocation of computer time.

Conflicts of Interest: The authors declare no conflicts of interest. The funders had no role in the design of the study; in the collection, analyses, or interpretation of data; in the writing of the manuscript; or in the decision to publish the results.

References

1. Londono, D.; Kuhs, W.F.; Finney, J.L. Enclathration of Helium in Ice II: The First Helium Hydrate. *Nature* **1988**, *332*, 141–142. [[CrossRef](#)]
2. Londono, D.; Kuhs, W.F.; Finney, J.L. Formation, Stability and Structure of Helium Hydrate at High Pressure. *J. Chem. Phys.* **1992**, *97*, 547–552. [[CrossRef](#)]
3. Loveday, J.S.; Nelmes, R.J. High-Pressure Gas Hydrates. *Phys. Chem. Chem. Phys.* **2008**, *10*, 913–1068. [[CrossRef](#)] [[PubMed](#)]
4. Kuhs, W.F.; Hansen, T.C.; Falenty, A. Filling Ices with Helium and the Formation of Helium Clathrate Hydrate. *J. Phys. Chem. Lett.* **2018**, *9*, 3194–3198. [[CrossRef](#)] [[PubMed](#)]

5. Arnold, G.P.; Wenzel, R.G.; Rabideau, S.W.; Nereson, N.G.; Bowman, A.L. Neutron Diffraction Study of Ice Polymorphs under Helium Pressure. *J. Chem. Phys.* **1971**, *55*, 589–595. [[CrossRef](#)]
6. Namiot, A.Y.; Bukhgalter, E.B. Clathrates formed by gases in ice. *J. Struct. Chem.* **1965**, *6*, 873–874. [[CrossRef](#)]
7. Kahane, A.; Klinger, J.; Philippe, M. Dopage Selectif De La Glace Monocristalline Avec De L'Helium Et Du Neon. *Solid State Commun.* **1969**, *7*, 1055–1056. [[CrossRef](#)]
8. Haas, J.; Bullemer, B.; Kahane, A. Diffusion de l'helium dans la glace monocristalline. *Solid State Commun.* **1971**, *9*, 2033–2035. [[CrossRef](#)]
9. Klinger, J. Thermal conductivity of ice doped with helium. *Solid State Commun.* **1975**, *16*, 961–963. [[CrossRef](#)]
10. Satoh, K.; Uchida, T.; Hondoh, T.; Mae, S. Diffusion coefficient and solubility measurements of noble gases in ice crystals. *Proc. NIPR Symp. Polar Meteorol. Glaciol.* **1996**, *10*, 73–81.
11. Lobban, C.; Finney, J.L.; Kuhs, W.F. The p-T Dependency of the Ice II Crystal Structure and the Effect of Helium Inclusion. *J. Chem. Phys.* **2002**, *117*, 3928–3934. [[CrossRef](#)]
12. Wang, Y.; Li, J.C. Diffuse neutron-scattering studies of ice Ih under high pressures. *Can. J. Phys.* **2003**, *81*, 409–413. [[CrossRef](#)]
13. Ildiyakov, A.V.; Manakov, A.Y.; Aladko, E.Y.; Kosyakov, V.I.; Shestakov, V.A. Solubility of Helium in Ice Ih at Pressures up to 2000 bar: Experiment and Calculations. *J. Phys. Chem. B* **2013**, *117*, 7756–7762. [[CrossRef](#)] [[PubMed](#)]
14. Malenkov, G.; Zheligovskaya, E. Dynamics of Some He and Ar Clathrate Hydrates. Computer Simulation Study. *J. Incl. Phenom. Macrocycl. Chem.* **2004**, *48*, 45–54. [[CrossRef](#)]
15. Belosludov, V.; Subbotin, O.; Bozhko, Y.; Belosludov, R.; Mizuseki, H.; Kawazoe, Y.; Fomin, V. Prediction of Structure, Composition and Phase Behavior of Helium Hydrates. In Proceedings of the 7th International Conference on Gas Hydrates (ICGH 2011), Edinburgh, UK, 17–21 July 2011; pp. 1–9. [[CrossRef](#)]
16. Belosludov, R.V.; Bozhko, Y.Y.; Subbotin, O.S.; Belosludov, V.R.; Mizuseki, H.; Kawazoe, Y.; Fomin, V.M. Stability and Composition of Helium Hydrates Based on Ices Ih and II at Low Temperatures. *J. Phys. Chem. C* **2014**, *118*, 2587–2593. [[CrossRef](#)]
17. Teeratchanan, P.; Hermann, A. Computational phase diagrams of noble gas hydrates under pressure. *J. Chem. Phys.* **2015**, *143*, 154507. [[CrossRef](#)]
18. Kaur, S.P.; Ramachandran, C.N. Host-guest and guest-guest interactions in noble gas hydrates. *Mol. Phys.* **2018**, *116*, 54–63. [[CrossRef](#)]
19. Papadimitriou, N.I.; Tsimpanogiannis, I.N.; Stubos, A.K.; Martin, A.; Rovetto, L.J.; Peters, C.J. Unexpected Behavior of Helium as Guest Gas in sII Binary Hydrates. *J. Phys. Chem. Lett.* **2010**, *1*, 1014–1017. [[CrossRef](#)]
20. Papadimitriou, N.I.; Tsimpanogiannis, I.N.; Stubos, A.K.; Martín, A.; Rovetto, L.J.; Florusse, L.J.; Peters, C.J. Experimental and Computational Investigation of the sII Binary He-THF Hydrate. *J. Phys. Chem. B* **2011**, *115*, 1411–1415. [[CrossRef](#)]
21. Ildiyakov, A.V.; Manakov, A.Y.; Zavjalov, A.P.; Bardakhanov, S.P. Gas Hydrate Formation by Methane-Helium Mixtures. *Chem. Eng. Technol.* **2011**, *34*, 1733–1738. [[CrossRef](#)]
22. Mondal, S.; Chattaraj, P.K. Noble gas encapsulation: Clathrate hydrates and their HF doped analogues. *Phys. Chem. Chem. Phys.* **2014**, *16*, 17943–17954. [[CrossRef](#)] [[PubMed](#)]
23. Salzmann, C.G. Advances in the experimental exploration of water's phase diagram. *J. Chem. Phys.* **2019**, *150*, 060901. [[CrossRef](#)] [[PubMed](#)]
24. Falenty, A.; Hansen, T.C.; Kuhs, W.F. Formation and properties of ice XVI obtained by emptying a type sII clathrate hydrate. *Nature* **2014**, *516*, 231–233. [[CrossRef](#)] [[PubMed](#)]
25. Liu, Y.; Zhao, T.; Ju, W.; Shi, S. Materials discovery and design using machine learning. *J. Mater.* **2017**, *3*, 159–177. [[CrossRef](#)]
26. Szczypiński, F.T.; Bennett, S.; Jelfs, K.E. Can we predict materials that can be synthesised? *Chem. Sci.* **2021**, *12*, 830–840. [[CrossRef](#)] [[PubMed](#)]
27. Mroz, A.M.; Posligua, V.; Tarzia, A.; Wolpert, E.H.; Jelfs, K.E. Into the Unknown: How Computation Can Help Explore Uncharted Material Space. *J. Am. Chem. Soc.* **2022**, *144*, 18730–18743. [[CrossRef](#)] [[PubMed](#)]
28. Roberts, J.; Zurek, E. Computational materials discovery. *J. Chem. Phys.* **2022**, *156*, 210401. [[CrossRef](#)]
29. Chang, C.; Deringer, V.L.; Katti, K.S.; Van Speybroeck, V.; Wolverton, C.M. Simulations in the era of exascale computing. *Nat. Rev. Mater.* **2023**, *8*, 309–313. [[CrossRef](#)]
30. Liu, T.; Lu, D.; Zhang, H.; Zheng, M.; Yang, H.; Xu, Y.; Luo, C.; Zhu, W.; Yu, K.; Jiang, H. Applying high-performance computing in drug discovery and molecular simulation. *Natl. Sci. Rev.* **2016**, *3*, 49–63. [[CrossRef](#)]
31. Penchoff, D.A.; Valeev, E.; Jagode, H.; Luszczek, P.; Danalis, A.; Bosilca, G.; Harrison, R.J.; Dongarra, J.; Windus, T.L. An Introduction to High Performance Computing and Its Intersection with Advances in Modeling Rare Earth Elements and Actinides. In *Rare Earth Elements and Actinides: Progress in Computational Science Applications*; ACS Publications: Washington, DC, USA, 2021; Chapter 1, pp. 3–53. [[CrossRef](#)]
32. Malyshkina, M.V.; Novikov, A.S. Modern Software for Computer Modeling in Quantum Chemistry and Molecular Dynamics. *Compounds* **2021**, *1*, 134–144. [[CrossRef](#)]
33. Zhang, J.; Chen, D.; Xia, Y.; Huang, Y.P.; Lin, X.; Han, X.; Ni, N.; Wang, Z.; Yu, F.; Yang, L.; et al. Artificial Intelligence Enhanced Molecular Simulations. *J. Chem. Theory Comput.* **2023**, *19*, 4338–4350. [[CrossRef](#)] [[PubMed](#)]
34. Bogojeski, M.; Vogt-Maranto, L.; Tuckerman, M.E.; Müller, K.R.; Burke, K. Quantum chemical accuracy from density functional approximations via machine learning. *Nat. Commun.* **2020**, *11*, 5223. [[CrossRef](#)]

35. Keith, J.A.; Vassilev-Galindo, V.; Cheng, B.; Chmiela, S.; Gastegger, M.; Müller, K.R.; Tkatchenko, A. Combining Machine Learning and Computational Chemistry for Predictive Insights Into Chemical Systems. *Chem. Rev.* **2021**, *121*, 9816–9872. [[CrossRef](#)] [[PubMed](#)]
36. Li, W.; Ma, H.; Li, S.; Ma, J. Computational and data driven molecular material design assisted by low scaling quantum mechanics calculations and machine learning. *Chem. Sci.* **2021**, *12*, 14987–15006. [[CrossRef](#)] [[PubMed](#)]
37. Hu, W.; Chen, M. Editorial: Advances in Density Functional Theory and beyond for Computational Chemistry. *Front. Chem.* **2021**, *9*, 705762. [[CrossRef](#)] [[PubMed](#)]
38. Yanes-Rodríguez, R.; Cabrera-Ramírez, A.; Prosmi, R. Delving into guest-free and He-filled sI and sII clathrate hydrates: A first-principles computational study. *Phys. Chem. Chem. Phys.* **2022**, *24*, 13119–13129. [[CrossRef](#)] [[PubMed](#)]
39. Yanes-Rodríguez, R.; Prosmi, R. Computational investigations of stable multiple cage occupancy He clathrate-like hydrostructures. *Phys. Chem. Chem. Phys.* **2023**, *25*, 16844–16855. [[CrossRef](#)]
40. Yanes-Rodríguez, R.; Prosmi, R. Analysing the stability of He-filled hydrates: How many He atoms fit in the sII crystal? *Phys. Chem. Chem. Phys.* **2023**.
41. del Rosso, L.; Celli, M.; Ulivi, L. New porous water ice metastable at atmospheric pressure obtained by emptying a hydrogen-filled ice. *Nat. Commun.* **2016**, *7*, 13394. [[CrossRef](#)]
42. Catti, M.; del Rosso, L.; Ulivi, L.; Celli, M.; Grazzi, F.; Hansen, T.C. Ne- and O₂-filled ice XVII: A neutron diffraction study. *Phys. Chem. Chem. Phys.* **2019**, *21*, 14671–14677. [[CrossRef](#)]
43. del Rosso, L.; Grazzi, F.; Celli, M.; Colognesi, D.; Garcia-Sakai, V.; Ulivi, L. Refined Structure of Metastable Ice XVII from Neutron Diffraction Measurements. *J. Phys. Chem. C* **2016**, *120*, 26955–26959. [[CrossRef](#)]
44. del Rosso, L.; Celli, M.; Colognesi, D.; Rudić, S.; English, N.J.; Burnham, C.J.; Ulivi, L. Dynamics of hydrogen guests in ice XVII nanopores. *Phys. Rev. Mater.* **2017**, *1*, 065602. [[CrossRef](#)]
45. Amos, D.M.; Donnelly, M.E.; Teeratchanan, P.; Bull, C.L.; Falenty, A.; Kuhs, W.F.; Hermann, A.; Loveday, J.S. A Chiral Gas–Hydrate Structure Common to the Carbon Dioxide–Water and Hydrogen–Water Systems. *J. Phys. Chem. Lett.* **2017**, *8*, 4295–4299. [[CrossRef](#)] [[PubMed](#)]
46. Zhu, X.L.; Yuan, Z.Y.; Jiang, L.; Zhang, K.; Wang, Z.R.; Luo, H.W.; Gu, Y.; Cao, J.W.; Qin, X.L.; Zhang, P. Computational analysis of vibrational spectrum and hydrogen bonds of ice XVII. *New. J. Phys.* **2019**, *21*, 043054. [[CrossRef](#)]
47. Pradana, I.P.; Mardiana, D.; Hakim, L. Carbon dioxide occupancies inside ice XVII structure from grand-canonical Monte Carlo simulation. *IOP Conf. Ser. Mater. Sci. Eng.* **2020**, *833*, 012035. [[CrossRef](#)]
48. Yanes-Rodríguez, R.; Arismendi-Arrieta, D.; Prosmi, R. He inclusion in ice-like and clathrate-like frameworks: A benchmark quantum chemistry study of guest–host interactions. *J. Chem. Inf. Model.* **2020**, *60*, 3043–3056. [[CrossRef](#)]
49. Cabrera-Ramírez, A.; Yanes-Rodríguez, R.; Prosmi, R. Computational density-functional approaches on finite-size and guest-lattice effects in CO₂@sII clathrate hydrate. *J. Chem. Phys.* **2021**, *154*, 044301. [[CrossRef](#)]
50. Kapil, V.; Schran, C.; Zen, A.; Chen, J.; Pickard, C.J.; Michaelides, A. The first-principles phase diagram of monolayer nanoconfined water. *Nature* **2022**, *609*, 512–516. [[CrossRef](#)]
51. Yanes-Rodríguez, R.; Prosmi, R. Assessment of DFT approaches in noble gas clathrate-like clusters: Stability and thermodynamics. *Phys. Chem. Chem. Phys.* **2022**, *24*, 1475–1485. [[CrossRef](#)]
52. Cabrera-Ramírez, A.; Prosmi, R. Modeling of Structure H Carbon Dioxide Clathrate Hydrates: Guest-Lattice Energies, Crystal Structure, and Pressure Dependencies. *J. Phys. Chem. C* **2022**, *126*, 14832–14842. [[CrossRef](#)]
53. Della Pia, F.; Zen, A.; Alfè, D.; Michaelides, A. DMC-ICE13: Ambient and high pressure polymorphs of ice from diffusion Monte Carlo and density functional theory. *J. Chem. Phys.* **2022**, *157*, 134701. [[CrossRef](#)] [[PubMed](#)]
54. Valdés, A.; Cabrera-Ramírez, A.; Prosmi, R. Confining CO₂ inside sI clathrate-hydrates: The impact of the CO₂-water interaction on quantized dynamics. *J. Comput. Chem.* **2023**, *44*, 1587–1598. [[CrossRef](#)]
55. Chaplin, M. Water Structure and Science. Available online: https://water.lsbu.ac.uk/water/water_structure_science.html (accessed on 29 September 2023).
56. Momma, K.; Izumi, F. VESTA 3 for three-dimensional visualization of crystal, volumetric and morphology data. *J. Appl. Crystallogr.* **2011**, *44*, 1272–1276. [[CrossRef](#)]
57. Giannozzi, P.; Baroni, S.; Bonini, N.; Calandra, M.; Car, R.; Cavazzoni, C.; Ceresoli, D.; Chiarotti, G.L.; Cococcioni, M.; Dabo, I.; et al. QUANTUM ESPRESSO: A modular and open-source software project for quantum simulations of materials. *J. Phys. Condens. Matter* **2009**, *21*, 395502. [[CrossRef](#)] [[PubMed](#)]
58. Giannozzi, P.; Andreussi, O.; Brumme, T.; Bunau, O.; Buongiorno Nardelli, M.; Calandra, M.; Car, R.; Cavazzoni, C.; Ceresoli, D.; Cococcioni, M.; et al. Advanced capabilities for materials modelling with Quantum ESPRESSO. *J. Phys. Condens. Matter* **2017**, *29*, 465901. [[CrossRef](#)]
59. Giannozzi, P.; Basergio, O.; Bonfá, P.; Brunato, D.; Car, R.; Carnimeo, I.; Cavazzoni, C.; de Gironcoli, S.; Delugas, P.; Ferrari Ruffino, F.; et al. Quantum ESPRESSO toward the exascale. *J. Chem. Phys.* **2020**, *152*, 154105. [[CrossRef](#)]
60. Perdew, J.P.; Yue, W. Accurate and simple density functional for the electronic exchange energy: Generalized gradient approximation. *Phys. Rev. B* **1986**, *33*, 8800. [[CrossRef](#)]
61. Perdew, J.P.; Burke, K.; Ernzerhof, M. Generalized Gradient Approximation Made Simple. *Phys. Rev. Lett.* **1996**, *77*, 3865. [[CrossRef](#)]
62. Zhang, Y.; Yang, W. Comment on “Generalized Gradient Approximation Made Simple”. *Phys. Rev. Lett.* **1998**, *80*, 890. [[CrossRef](#)]

63. Johnson, E.R.; Becke, A.D. A post-Hartree-Fock model of intermolecular interactions. *J. Chem. Phys.* **2005**, *123*, 024101. [[CrossRef](#)]
64. Becke, A.D.; Johnson, E.R. Exchange-hole dipole moment and the dispersion interaction. *J. Chem. Phys.* **2005**, *122*, 154104. [[CrossRef](#)] [[PubMed](#)]
65. Grimme, S.; Jens, A.; Ehrlich, S.; Krieg, H. A Consistent and Accurate Ab Initio Parametrization of Density Functional Dispersion Correction (DFT-D) for the 94 Elements H-Pu. *J. Chem. Phys.* **2010**, *132*, 154104. [[CrossRef](#)] [[PubMed](#)]
66. Universität-Bonn. D4—A Generally Applicable Atomic-Charge Dependent London Dispersion Correction. Available online: <https://github.com/dftd4/dftd4> (accessed on 20 July 2023).
67. Caldeweyher, E.; Bannwarth, C.; Grimme, S. Extension of the D3 dispersion coefficient model. *J. Chem. Phys.* **2017**, *147*, 034112. [[CrossRef](#)]
68. Caldeweyher, E.; Ehlert, S.; Hansen, A.; Neugebauer, H.; Spicher, S.; Bannwarth, C.; Grimme, S. A generally applicable atomic-charge dependent London dispersion correction. *J. Chem. Phys.* **2019**, *150*, 154122. [[CrossRef](#)] [[PubMed](#)]
69. Caldeweyher, E.; Mewes, J.M.; Ehlert, S.; Grimme, S. Extension and evaluation of the D4 London-dispersion model for periodic systems. *Phys. Chem. Chem. Phys.* **2020**, *22*, 8499–8512. [[CrossRef](#)]
70. Klimeš, J.; Bowler, D.R.; Michaelides, A. Chemical accuracy for the van der Waals density functional. *J. Phys. Condens. Matter* **2009**, *22*, 022201. [[CrossRef](#)]
71. Dion, M.; Rydberg, H.; Schröder, E.; Langreth, D.C.; Lundqvist, B.I. Van der Waals Density Functional for General Geometries. *Phys. Rev. Lett.* **2004**, *92*, 246401. [[CrossRef](#)]
72. Lee, K.; Murray, E.D.; Kong, L.; Lundqvist, B.I.; Langreth, D.C. Higher-accuracy van der Waals density functional. *Phys. Rev. B* **2010**, *82*, 081101. [[CrossRef](#)]
73. Blöchl, P.E. Projector augmented-wave method. *Phys. Rev. B* **1994**, *50*, 17953–17979. [[CrossRef](#)]
74. Monkhorst, H.J.; Pack, J.D. Special points for Brillouin-zone integrations. *Phys. Rev. B* **1976**, *13*, 5188–5192. [[CrossRef](#)]
75. Makov, G.; Payne, M.C. Periodic boundary conditions in ab initio calculations. *Phys. Rev. B* **1995**, *51*, 4014–4022. [[CrossRef](#)]
76. Santra, B.; Klimeš, J.; Tkatchenko, A.; Alfè, D.; Slater, B.; Michaelides, A.; Car, R.; Scheffler, M. On the accuracy of van der Waals inclusive density-functional theory exchange-correlation functionals for ice at ambient and high pressures. *J. Chem. Phys.* **2013**, *139*, 154702. [[CrossRef](#)] [[PubMed](#)]
77. Murnaghan, F.D. The Compressibility of Media under Extreme Pressures. *Proc. Natl. Acad. Sci. USA* **1944**, *30*, 244–247. [[CrossRef](#)] [[PubMed](#)]
78. Fortes, A.D.; Wood, I.G.; Brodholt, J.P.; Vočadlo, L. Ab initio simulation of the ice II structure. *J. Chem. Phys.* **2003**, *119*, 4567–4572. [[CrossRef](#)]
79. Gagnon, R.E.; Kiefte, H.; Clouter, M.J.; Whalley, E. Acoustic velocities and densities of polycrystalline ice Ih, II, III, V, and VI by Brillouin spectroscopy. *J. Chem. Phys.* **1990**, *92*, 1909–1914. [[CrossRef](#)]
80. Fortes, A.D.; Wood, I.G.; Alfredsson, M.; Vočadlo, L.; Knight, K.S. The incompressibility and thermal expansivity of D₂O ice II determined by powder neutron diffraction. *J. Appl. Crystallogr.* **2005**, *38*, 612–618. [[CrossRef](#)]
81. Ohto, T.; Dodia, M.; Xu, J.; Imoto, S.; Tang, F.; Zysk, F.; Kühne, T.D.; Shigeta, Y.; Bonn, M.; Wu, X.; et al. Accessing the Accuracy of Density Functional Theory through Structure and Dynamics of the Water–Air Interface. *J. Phys. Chem. Lett.* **2019**, *10*, 4914–4919. [[CrossRef](#)]
82. Yu, X.; Zhu, J.; Du, S.; Xu, H.; Vogel, S.C.; Han, J.; Germann, T.C.; Zhang, J.; Jin, C.; Francisco, J.S.; et al. Crystal structure and encapsulation dynamics of ice II-structured neon hydrate. *Proc. Natl. Acad. Sci. USA* **2014**, *111*, 10456–10461. [[CrossRef](#)]

Disclaimer/Publisher’s Note: The statements, opinions and data contained in all publications are solely those of the individual author(s) and contributor(s) and not of MDPI and/or the editor(s). MDPI and/or the editor(s) disclaim responsibility for any injury to people or property resulting from any ideas, methods, instructions or products referred to in the content.